IOP Publishing Biofabrication 16 (2024) 045030 https://doi.org/10.1088/1758-5090/ad6f46

Biofabrication

RECEIVED
28 December 2023

REVISED
4 August 2024

ACCEPTED FOR PUBLICATION
14 August 2024

PUBLISHED
23 August 2024

PAPER

In vitro three-dimensional volumetric printing of vitreous body models using decellularized extracellular matrix bioink

Jeong Sik Kong[1,2,4], **Joeng Ju Kim**[1,2,4], **Leonardo Riva**[3,4], **Paola Serena Ginestra**[3,*] **and Dong-Woo Cho**[1,2,*]

[1] Department of Mechanical Engineering, Pohang University of Science and Technology (POSTECH), Pohang, Kyungbuk 37673, Republic of Korea
[2] POSTECH-Catholic Biomedical Engineering Institute, POSTECH, Pohang, Kyungbuk 37673, Republic of Korea
[3] Department of Industrial and Mechanical Engineering, University of Brescia, Via Branze 38, 25125 Brescia, Italy
[4] These authors contributed equally to this work.
[*] Authors to whom any correspondence should be addressed.

E-mail: paola.ginestra@unibs.it and dwcho@postech.ac.kr

Keywords: 3D cell printing, decellularized extracellular matrix bioink, volumetric vitreous body printing, eye *in vitro* model, bioink

Supplementary material for this article is available online

Abstract

Hyalocytes, which are considered to originate from the monocyte/macrophage lineage, play active roles in vitreous collagen and hyaluronic acid synthesis. Obtaining a hyalocyte-compatible bioink during the 3D bioprinting of eye models is challenging. In this study, we investigated the suitability of a cartilage-decellularized extracellular matrix (dECM)-based bioink for printing a vitreous body model. Given that achieving a 3D structure and environment identical to those of the vitreous body necessitates good printability and biocompatibility, we examined the mechanical and biological properties of the developed dECM-based bioink. Furthermore, we proposed a 3D bioprinting strategy for volumetric vitreous body fabrication that supports cell viability, transparency, and self-sustainability. The construction of a 3D structure composed of bioink microfibers resulted in improved transparency and hyalocyte-like macrophage activity in volumetric vitreous mimetics, mimicking real vitreous bodies. The results indicate that our 3D structure could serve as a platform for drug testing in disease models and demonstrate that the proposed printing technology, utilizing a dECM-based bioink and volumetric vitreous body, has the potential to facilitate the development of advanced eye models for future studies on floater formation and visual disorders.

1. Introduction

Vitreous humor occupies approximately 80% of the eye volume and fills the space between the lens and retina [1]. It comprises a transparent and fragile hydrogel composed of approximately 99% water [2]; other major constituents include collagen fibrils, hyaluronic acid, hyalocytes, inorganic salts, and lipids [3]. Vitreous humor absorbs and dampens external forces, reduces mechanical deformation of the eye, acts as a metabolic buffer, and allows light to reach the retina while maintaining transparency [4]. These features make vitreous humor an active component of the eye physiology and not just a filler [5]. However, the vitreous body undergoes natural aging owing to the biochemical changes occurring inside it. These changes affect the collagen content and viscosity of the vitreous gel, resulting in a gradual liquefaction of the gels [6]. Vitreous liquefaction occurs because hyaluronic acid separates from the collagen fibers. Subsequently, the fibers aggregate and the entrapped aqueous medium is released [7]. Vitreous liquefaction can lead to posterior vitreous detachment (PVD), wherein the vitreous gel detaches from the retina [8]; this is one of the primary causes of vitreous opacity, retinal detachment (RD), and macular holes (MHs). Floaters are common eye complaints that are typically described as bubbles, dark spots, or bugs in the visual field [9]. While generally benign, floaters can interfere with the vision in some cases, cause physiological stress [10], and negatively impact the quality of life.

Hyalocytes are mononuclear cells located in the posterior vitreous cortex [6], and they are derived from the monocyte/macrophage lineage [11]. Hyalocytes perform various functions within the eye, including extracellular matrix (ECM) synthesis [12], and they are reported to be responsible for vitreous collagen and hyaluronic acid synthesis [11, 13]. Furthermore, they stimulate cell migration and proliferation as well as gel contraction [14]. Therefore, we hypothesized that hyalocytes play a role in floater and vitreous liquefaction, causing PVD.

Some studies have presented two-dimensional (2D) culture systems for hyalocytes to study vitreous diseases [15–17]. To the best of our knowledge, a three-dimensional (3D) eye model mimicking the volumetric vitreous body environment has not been developed.

Recent advancements in additive manufacturing have enabled the development of new methods and tools for studying 3D *in vitro* models [18]. 3D bioprinting is a branch of additive manufacturing that involves the printing of biomaterials, cells, and biomolecules [19] to develop structures that can mimic the human body [20]. Extrusion-based printing, one of the most commonly used bioprinting methods, involves the extrusion of a cell-laden hydrogel through a nozzle via compressed air or a plunger. For the 3D bioprinting of a vitreous body, a hyalocyte-specific bioink providing a vitreous body-like microenvironment must be developed for accurate recapitulation; however, no such study on bioinks for vitreous body printing has been conducted.

Several natural and synthetic hydrogels have been tested as vitreous substitutes [5, 7, 21]. However, most studies have focused on the development of the vitreous tamponade, and only a few studies have focused on the compatibility of hyalocytes and hydrogels. Recently, a new type of hydrogel bioink, called a decellularized extracellular matrix (dECM) hydrogel, was developed. As the name suggests, these hydrogels are based on decellularized biological tissues. Although they may have poor printability owing to a low viscosity caused by protein damage during decellularization, they can provide the ideal conditions for the native matrix. Therefore, dECM hydrogels are widely used in 3D bioprinting [22]. Vitreous body dECM is the most suitable for producing a vitreous body-specific bioink. However, 99% of the vitreous body is composed of water. Therefore, obtaining a sufficient amount of dECM from the vitreous body is difficult.

The natural composition of the cartilage matrix is similar to that of the vitreous gel [23], and obtaining a large amount of cartilage dECM is facile. Thus, we hypothesize that a cartilage dECM can be a suitable bioink for 3D culture of hyalocytes.

In this study, we aimed to investigate the suitability of a cartilage dECM-based bioink (CDB) as a vitreous substitute for eye models intended for the study of floater formation and vitreous liquefaction caused by hyalocytes, which can be influenced by volumetric mechanical load or exposure to light. Biocompatibility, transparency, rheological, and swelling tests were performed, which demonstrated the suitability of the CDB for the 3D bioprinting of vitreous body model. We also developed a 3D printing strategy to create volumetric vitreous bodies on a centimeter scale. This strategy involves using macrophage-laden CDB and it consists of an interconnected porous structure (figure 1). The porous design improved the cell viability and transparency of the volumetric structure. Moreover, the CDB and interconnected porous design supported the hyalocyte-like activity of the macrophages, which is related to the physiological function of the vitreous body. Hence, the developed bioink and volumetric vitreous body printing technology can be used for hyalocyte printing and volumetric eye model fabrication, enabling studies on vitreous diseases.

2. Materials and methods

2.1. CDB preparation

For cartilage dECM preparation, the cartilage, which was dissected from porcine bones acquired from a local market, was rinsed with 1× phosphate-buffered saline (PBS) for 1 h. The tissues were cut into small pieces, which were subjected to six cycles of freezing (−80 °C) and thawing (37 °C). The tissues were then submerged in a 0.25% (w/v) trypsin/PBS solution for 24 h in an incubator at 37 °C, washed with a hypertonic buffer (1.5 M NaCl and 50 mM Tris-HCL; pH 7.6) for 12 h, and treated with 50 U ml^{-1} of DNase/1 U ml^{-1} of RNase A in 10 mM Tris-HCL with a pH of 7.5 at 37 °C for 4 h. To remove the enzymes, the samples were placed in a 10 mM Tris-HCL solution for 24 h, followed by treatment with 1% (v/v) Triton X-100 in PBS for 24 h. Finally, the decellularized tissues were rinsed in 1× PBS for six cycles of 8 h each and freeze-dried [24].

For CDB preparation, 10.5 mg of dECM and 4.5 mg of collagen type 1 were dissolved in 0.8 ml of 0.5 M acetic acid (80% of the final volume) with pepsin (10% of the dECM weight). The solution was stirred at 550 rpm at room temperature for 2 d until complete dissolution. Next, 10 M NaOH was gradually added until the pH level reached 7 after the addition of 10× PBS (10% of the final volume). Distilled water (DW) was added to achieve the final volume.

In the case of the collagen type-1 hydrogel group, 15 mg of collagen type 1 was dissolved in 0.8 ml of 0.5 M acetic acid with pepsin, and the obtained solution was processed in the same manner as that for CDB preparation.

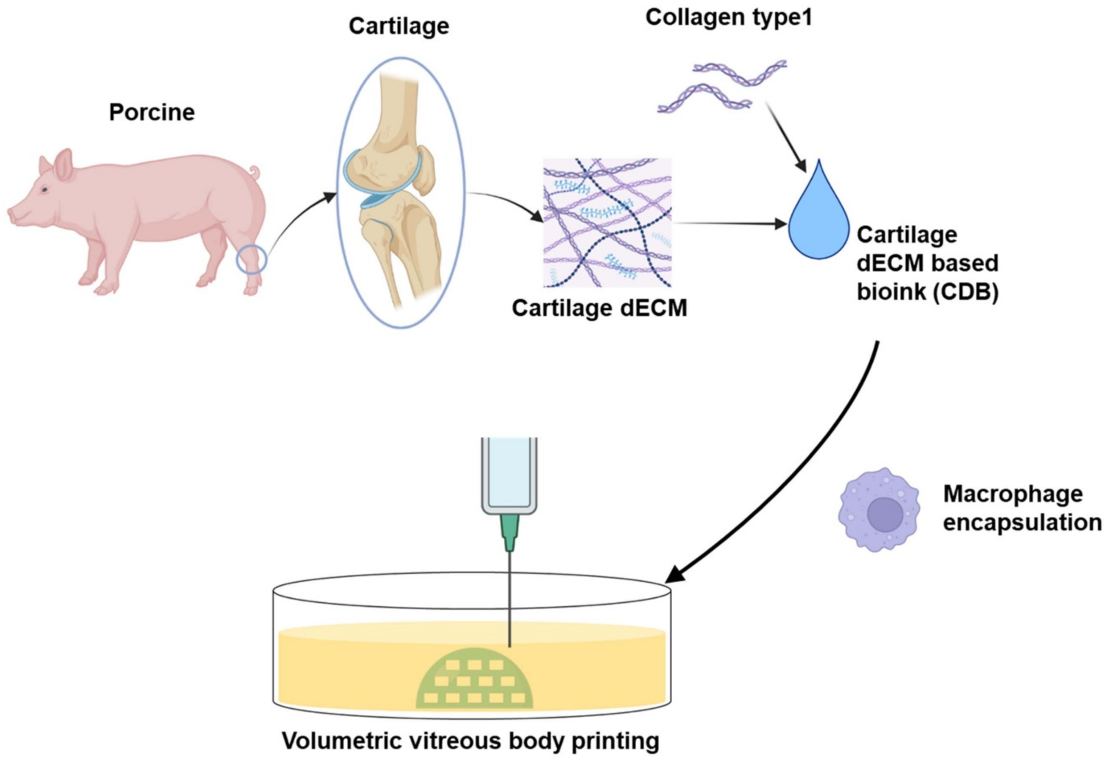

Figure 1. Schematic of CDB development and the fabrication of a volumetric vitreous body structure via 3D bioprinting. dECM, decellularized extracellular matrix; CDB, cartilage dECM-based bioink; 3D, three-dimensional.

2.2. Supporting bath preparation

A previously developed alginate-based solution was used as the supporting bath, comprising 6% of gelatin, 3% of alginate, 10% of polyvinyl alcohol (PVA), and 30 mM of $CaCl_2$ in DW [25]. Briefly, the gelatin, sodium alginate, and PVA were added without mixing to half of the required DW, placed in an oven at 60 °C for 4 h, and sterilized in an autoclave. When the solution was warm, $CaCl_2$ (diluted in the remaining DW) was added and mixed thoroughly. Subsequently, centrifugation at 1000 rpm for 30 min was conducted to remove any bubbles.

2.3. Bioprinting

Printing was performed using a 3DX Printer (T&R Biofab). The printing pressure (P), speed (s), and layer thickness (lt) were varied, and the final 3D structures were built using the optimal parameters ($P = 20$ kPa; $s = 300$ mm min^{-1}; lt = 0.75 mm). CDB-encapsulating macrophages (3×10^6 cells ml^{-1}) were maintained at 4 °C during printing, while the building plate was maintained at 30 °C. A 25 G needle (0.25 mm; Musashi Engineering, Inc.) was used for printing, which was performed in petri dishes containing a supporting bath.

The resulting 3D structures were dome-shaped with a diameter and height of 10 and 5 mm, respectively. Four different types of structures were fabricated for comparison: a bulky dome (Bulky/Dome), a porous dome with thick fiber (Thick/Dome), a porous dome with thin fiber (Thin/Dome), and a porous cuboid with thin fiber (Thin/Cuboid). The building paths were set at a 2 mm grid for the Thick/Dome, Thin/Dome, and Thin/Cuboid structures, and at a 0.68-mm grid for the Bulky/Dome type. The printing speeds were adjusted accordingly: 300 mm min^{-1} for the Bulky/Dome, Thin/Dome, and Thin/Cuboid, and 150 mm min^{-1} for the Thick/Dome. The pressure ($P = 20$ kPa) and layer thickness (lt = 0.75 mm) remained equal for all printing groups. Thin/Cuboid had dimensions of 10 mm wide by 10 mm long by 5 mm high. After printing, the samples were placed in an incubator for crosslinking. Subsequently, the supporting bath was removed using a scoop and washed with PBS.

2.4. Cell culture

Human monocytic cell lines (THP-1; ATCC, USA) were grown in a high-glucose Dulbecco's modified Eagle's medium (DMEM) (Hyclone, USA). Human retinal pigment epithelial cells (HRPEs; ARPE-19; ATCC, USA) and human lens epithelial cells (HLEpiCs; ScienCell, USA) were grown in DMEM/F12 (Gibco, USA). The media were supplemented with 1% penicillin/streptomycin (Gibco, USA) and 10% fetal bovine serum (FBS; Gibco, USA). The cells were grown in a humidified atmosphere with 5% CO_2 at 37 °C, and the culture medium was replaced every 2 d. When the cells approached 80% confluence, they were removed from the culture dish using 0.25% trypsin–ethylenediaminetetraacetic acid (Sigma–Aldrich, USA) for 3 min, followed by centrifugation at 1300 rpm for 3 min at 23 °C. The supernatant was discarded, and the cell concentration was determined. The required concentration of cells was then either suspended in a fresh medium for further culture or encapsulated in hydrogels for the experiments as required.

2.5. Macrophage differentiation

To promote the differentiation of macrophages from THP-1 cells, a specific protocol was followed. Briefly, THP-1 cells were cultured in high glucose–DMEM supplemented with 1% penicillin/streptomycin (Gibco, USA) and 10% FBS (Gibco, USA) until they reached a concentration of 1×10^5 cells ml^{-1}. Subsequently, 100 ng ml^{-1} of phorbol 12-myristate 13-acetate (PMA; P8139, Sigma Aldrich, USA) was added to the medium for 48 h to induce differentiation into adherent macrophages; the nonadherent cells were removed by washing with 1× PBS. Subsequently, the medium was replaced with new high-glucose DMEM for 72 h to grow the adherent macrophages. To activate the macrophages, each scaffold was treated with 20 ng ml^{-1} interferon-gamma (IFN-γ; 285-IF, R&D system, USA) and 10 pg ml^{-1} lipopolysaccharide (LPS; Sigma–Aldrich, USA).

2.6. Biocompatibility tests

Biocompatibility was evaluated using live/dead and CCK8 assays. A total of 3×10^6 cells ml^{-1} were mixed with the 1.5% collagen type-1 hydrogel or CDB. The hydrogels were then crosslinked in an incubator.

2.6.1. Live/dead

On days 1, 4, and 7, the medium was removed from the wells, and the samples were washed twice with 1× PBS. Next, 1 ml of l d^{-1} solution was added to each well, and the samples were incubated for 30 min to induce a reaction. The samples were then observed using a confocal microscope (Zeiss, LSM 900). In the live/dead assay, viability was quantified as the ratio between the number of live cells and the sum of live plus dead cells, where the cells were counted using the ImageJ software.

2.6.2. CCK8

On days 1, 4, and 7, the medium was removed from the wells, and the hydrogel was washed twice with 1× PBS. Next, 500 μl of the CCK8 solution was added to each well, and the samples were incubated for 3 h to induce a reaction. Subsequently, 100 μl of the medium from each sample was pipetted into a 96 well plate. Analyses were performed using a microplate reader (enzyme-linked immunosorbent assay (ELISA) reader) at a wavelength of 450 nm.

2.6.3. Ki67-labeled cell counting

Ki67-expressing cells were counted using the ImageJ software after examining the immunostaining via a confocal microscope (LSM 800; Carl Zeiss Microscopy, Germany).

2.7. Rheological analysis of bioinks

Using a Discovery Hybrid Rheometer-2 (TA Instruments, USA) with a steel cone plate geometry (diameter, 20 mm), the crosslinked hydrogels were subjected to rheological tests, including the evaluation of the gelation kinetics, viscosity, and dynamic modulus. Initially, 1.5% collagen and CDB were prepared in a non-gelation state within a temperature-controlled environment maintained at 4 °C. Subsequently, 100 μl of each bioink was extracted with a viscous pipette and directly loaded onto the rheometer plate. Sample preparation was completed by gently pressing the bioink using a steel cone plate with a diameter of 20 mm until the thickness reached 50 μm. To conduct shear viscosity testing, the shear rate was increased linearly from 10^{-2} to $10^3\ \text{s}^{-1}$ at 4 °C while maintaining an appropriate temperature for printing using a non-gelation bioink. The gelation kinetics were assessed by performing an oscillatory temperature sweep test, with temperatures ranging from 4 °C to 37 °C, using a 5 °C min^{-1} ramp and then holding at 37 °C for 30 min. An oscillatory frequency-sweep test was conducted to estimate the dynamic profile of each bioink, with the bioinks being fully crosslinked before performing the examination on a rheometer plate for 30 min at 37 °C. The storage (G') and loss (G'') moduli were recorded under 2% strain over a frequency range of 10^{-1}–10^2 rad s^{-1}, and all experiments were conducted in triplicates.

2.8. Compression test of 3D printed constructs

Compression testing was conducted at a displacement rate of 0.4 mm min^{-1}, using a MicroTester G2 (CellScale). After attaching the beam to the samples, measurements were recorded by the MicroTester G2 software.

2.9. Transparency examination

Transparency examinations were conducted qualitatively and quantitatively. The qualitative test was conducted by spreading 150 μl of the hydrogel in a petri dish, allowing crosslinking, and placing it over a printed text. A quantitative test was performed by measuring the light transmittance using a spectrometer (SpectraMax Plus 384, USA). Each hydrogel was placed in a well of a 96 well plate at various heights (100, 400, 700, and 1000 μm) and crosslinked in an incubator at 37 °C. After placing the well plate in the spectrometer, the light absorption values were measured over a wavelength range of 300–800 nm. The light transmittance (T) values were derived by calculating the measured light absorbance (A) using the following equation:

$$T(\%) = \frac{1}{10^{A}} \times 100$$

2.10. Swelling ratio

The swelling ratio was measured using the following equation:

$$\text{Swelling ratio} = \frac{\text{Ws} - \text{Wd}}{\text{Wd}} \times 100 \qquad (1)$$

where Wd and Ws are the weights of the dried and swollen samples, respectively. To measure the weights, 500 μl of the hydrogel was placed in previously weighed conical tubes. The samples were freeze-dried after crosslinking in an incubator. The tubes containing the dried hydrogels were weighed again, and Wd was calculated as the difference between the two weights (weights of an empty tube and a dried hydrogel-containing tube). Subsequently, 1 ml of PBS was added to each tube to be absorbed by the hydrogel and maintained at 37 °C for 24 h. The Ws was measured after removing excess PBS from the tubes; Ws was obtained from the difference in the weights of the filled and empty tubes.

2.11. Immunofluorescence staining

Immunostaining was performed to confirm the expression of proteins in each tissue sample. The samples were harvested and placed in 4% paraformaldehyde (PFA; Chembio, South Korea) for 30 min for fixation, followed by washing with 1× PBS solution three times. The fixed samples were rapidly permeabilized with 0.1% Triton X-100 in PBS for 5 min, followed by washing with 1× PBS solution three times. After being blocked with 1% BSA (VWR Life Science, USA) in PBS for 30 min at room temperature, the samples were washed three times and incubated overnight at 4 °C with primary antibodies (1:100, anti-Ki67, ab15580, Abcam; anti-CD74, ab289885, Abcam; anti-CD68, MA5-13324, Invitrogen; anti-TGF beta-2, MA5-37505, Invitrogen; anti-fibronectin, ab23750, Abcam; anti-RPE65, ab231782, Abcam; anti-alpha smooth muscle actin, ab7817, Abcam; anti-E cadherin, ab231303, Abcam) against the targeted proteins of each tissue. The samples were washed with 1× PBS and treated with Alexa-405, Alexa-488, and Alexa-594 secondary antibodies (1:200, Thermo Fisher Scientific, USA) for 1 h, followed by treatment with 4′,6-diamidino-2-phenylindole (GBI Labs, USA) for 5 min at room temperature.

For histological staining, specimens in 4% PFA (Chembio, South Korea) were embedded in paraffin and cut into 15 μm thick slices using a Zeiss microtome. Rehydrated sections were used for the immunofluorescence staining of Ki67, following the aforementioned procedures.

2.12. Analytical measurements of cell secretomes

On day 9, the cell culture supernatant was collected and the levels of interleukin-6 (IL-6), C-X-C motif chemokine ligand 8/Interleukin-8 (CXCL8/IL-8) and tumor necrosis factor-α (TNF-α) in the supernatant were quantified using standard ELISA kits (R&D Systems, USA), following the manufacturer's instructions.

2.13. Gene expression analysis

To extract the total ribonucleic acid (RNA), cell samples cultured in each experiment were collected and lysed using RNAiso (Takara, Japan). Samples dissolved in RNAiso were purified and washed in the order of chloroform, isopropanol, and 75% ethanol to collect pure RNA. The purity and concentration of the extracted RNA were assessed using a NanoDrop instrument. A total of 1 μg of the harvested RNA was reverse-transcribed into complementary deoxyribonucleic acid (cDNA) using a cDNA synthesis kit (#K1642, Thermo Fisher Scientific, USA) following the manufacturer's instructions. The resulting cDNA was used as a template for quantitative real-time polymerase chain reaction (qRT-PCR) with the gene expression of markers for each experiment analyzed using the SYBR-green PCR Master Mix (Applied Biosystems, USA) on a StepOne Plus Real-Time PCR System (Thermo Fisher Scientific, USA). The primers (table S1) for glyceraldehyde-3-phosphate dehydrogenase (GAPDH); cluster of differentiation 74 (CD74); secreted phosphoprotein 1 (SPP1); CXCL8; C-X3-C motif chemokine receptor 1 (CX3CR1); transforming growth factor-beta 2 (TGF-β2); and CD68, fibronectin, RPE65, E-cadherin, and alpha-smooth muscle actin (α-SMA) were designed using the National Centre for Biotechnology Information public gene database. All primers were purchased from Pioneer (Seoul, Republic of Korea). Gene expression levels were normalized to those of GAPDH, and the relative transcriptional levels of target messenger RNAs (mRNAs) were evaluated using the $2^{-\Delta\Delta CT}$ method.

2.14. Refractive index measurement

The refractive index was measured using a digital refractometer (Sugar-2 Plus, CAS, Republic of Korea). The zero point of the machine was adjusted using DW. Next, the samples of each experimental group (native porcine vitreous body, CDB 3D dome cell (−), and CDB 3D dome cell (+) groups) were placed on the sample plate; the cover of the machine was closed and the read button was pressed to measure the refractive index of the sample. The refractive index (n) was automatically calculated by the machine and presented as a value on the liquid crystal display screen. We performed the measurements three times for each experimental group to obtain the mean and standard deviation values of the refractive index.

2.15. Preparation for vitreous body disease *in vitro* model and drug test

To simulate vitritis, a disease affecting the vitreous body, an *in vitro* model was created following the process outlined below (figure S5(a)). Initially, a standard 3D CDB porous dome was fabricated using 3D bioprinting, and the structure was stabilized. Treatment with 20 ng ml^{-1} interferon-gamma (IFN-γ; 285-IF, R&D Systems, USA) and 10 pg ml^{-1} lipopolysaccharide (LPS; Sigma-Aldrich, USA) was administered for one day to activate macrophages. Subsequently, an acute inflammatory environment was induced by exposure to 20 ng ml^{-1} TNF-alpha (GF023, Sigma-Aldrich, USA) for two days, thus creating the vitritis *in vitro* model. Following this, the model's suitability as a drug testing platform was verified by treating it with 50 ng ml^{-1} of the anti-inflammatory drug dexamethasone (Dexa; 265005, Sigma-Aldrich, USA) for a period of five days. Immunofluorescence staining and qRT-PCR analyses were conducted on samples collected on Day 7 to assess the expression levels of relevant markers (figures S5(b) and (c)).

2.16. Statistical analysis

The data were plotted as mean ± standard deviation values. A multiple t-test was conducted to determine the statistical significance of the experimental and control groups. Each experiment was repeated thrice to ensure that the results were comparable. The significance was determined based on the following thresholds: $^{*}p < 0.05$, $^{**}p < 0.01$, $^{***}p < 0.001$, and $\#p < 0.0001$.

3. Results

3.1. Development and characterization of the CDB for 3D macrophage culture

A pure cartilage-derived dECM (cdECM) bioink was prepared using our decellularization protocol [24]. However, the pure cdECM bioink has low collagen type-1 content, which is directly involved in crosslinking [26]. Additionally, the cross-linked cdECM bioink occasionally experienced collapse during culture due to batch variation. To address these issues, the CDB was formulated by blending collagen type 1 with the pure cdECM bioink, ensuring a stable cross-linking reaction regardless of batch variation (mixing ratio of pure cdECM bioink to collagen type 1 = 7:3). Prior studies have incorporated collagen type 1 into dECM bioink for stable cross-linking, demonstrating that functional superiority is maintained even with the addition of collagen type 1 [27–29]. Consequently, we verified that the CDB remained in a fluid state at 4 °C, exhibited crosslinking behavior upon incubation at 37 °C, and maintained 3D integrity stably (figure 2(a)).

Using various validation methods, we confirmed the possibility of using the CDB as a bioink for fabricating vitreous structures via a functional comparison with the collagen type 1 hydrogel. Collagen is widely used in vitreous structure fabrication and is generally used for 3D bioprinting [15, 30]. To confirm the characteristics of collagen type 1, the main biomaterials of the CDB, HRPEs and HLEpiCs, were cultured on 1.5% collagen type 1–coated culture dishes for 7 d, and their respective functions were confirmed. In both HRPEs and HLEpiCs, we found almost no expression of epithelial–mesenchymal transition (EMT) markers, including fibronectin and α-SMA, and RPE65 (an HRPE cell marker) and E-cadherin (an epithelial cell marker) were strongly expressed (figure S1(a)). These results suggest that the EMT process did not progress in each cell and that normal cell function was maintained. Furthermore, we confirmed that the cell function was enhanced and that the conversion to EMT was reduced in HRPEs and HLEpiCs exposed to collagen type 1 (figure S1(b)).

To confirm the feasibility of using the CDB as a bioink for 3D bioprinting, its rheological properties were measured. In both the CDB and collagen groups, the viscosity of the bioink decreased as the shear rate increased (figure 2(b)). When the shear rate changed from 0.139 to 1000 s^{-1}, the CDB viscosity decreased linearly from 8.043 to 0.106 Pa·s, and the viscosity of collagen type 1 hydrogel also decreased linearly from 11.428 to 0.061 Pa·s. This linear decrease indicated that both biomaterials exhibited shear-thinning behavior, which is essential for reducing the shear stress generated during extrusion-based bioprinting.

When the temperature was changed from 4 °C to 37 °C at a rate of 5 °C min^{-1}, the complex modulus of the CDB changed rapidly from 13.624 to 126.597 Pa and that of the collagen type 1 hydrogel changed from 11.511 to 138.150 Pa (figure 2(c)). Moreover, when the temperature was maintained at 37 °C, the complex modulus of the CDB increased to 165.063 Pa, and the complex modulus of the collagen type 1 hydrogel decreased to 54.429 Pa, leading to saturation. These results suggest that a gel–sol transition occurred in both biomaterials with thermal-crosslinking at 37 °C. This gel–sol transition phenomenon of the biomaterial is essential for the structure to maintain a specific shape.

When the angular frequency was changed from 0.1 to 100 rad s^{-1} at 37 °C to simulate shear stress, the storage modulus of the CDB increased from 30.967 to 103.291 Pa and the loss modulus of the CDB increased from 8.987 to 49.316 Pa (figure 2(d)). Furthermore, under the same conditions, the storage modulus of the collagen type 1 hydrogel increased from 8.342 to 21.902 Pa and the loss modulus of the collagen type 1 hydrogel increased from 2.417 to 14.107 Pa (figure 2(d)). For both biomaterials, the finding that the storage modulus remains greater

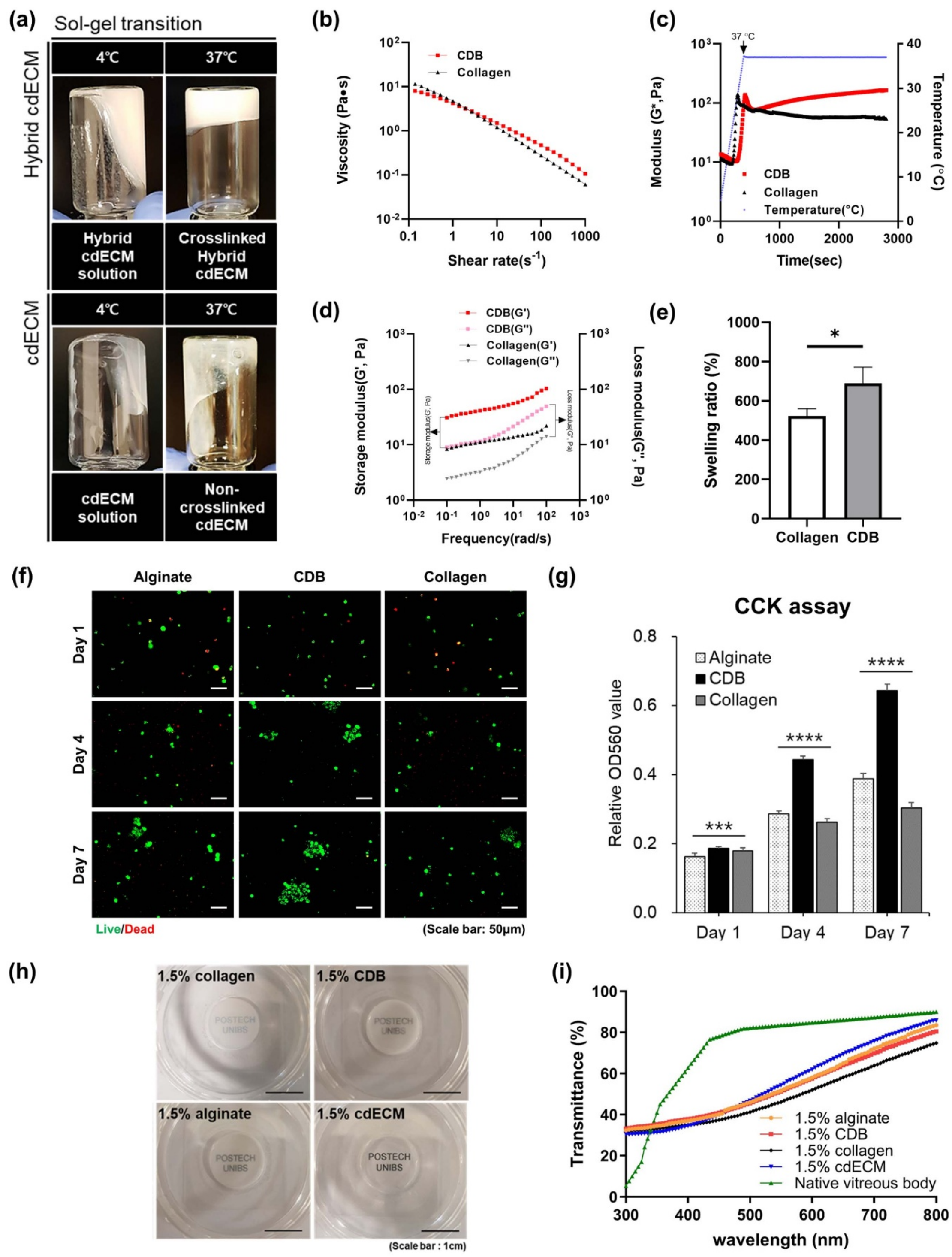

Figure 2. Comparative functional evaluation of CDB with various hydrogels. (a) Photographs of the CDB and cdECM bioinks. Rheological properties of the CDB: (b) viscosity, (c) gelation kinetics, and (d) complex modulus. (e) Swelling ratio of the CDB. (f) Live/dead stained images captured on days 1, 4, and 7. (g) CCK assay results. Determination of (h) transparency and (i) transmittance. The data are compared using student's t-test; significant differences are indicated as follows: $^{*}p < 0.05$, $^{**}p < 0.01$, $^{***}p < 0.001$, and $\# \, p < 0.0001$ ($n = 3$). CdECM, cartilage decellularized extracellular matrix; CDB, cartilage dECM–based bioink.

than the loss modulus under all shear stress conditions indicates that they maintain their gel form even when shear stress is applied. Based on these results, we inferred that the structure fabricated using the CDB can be maintained even when liquid (such as media) flow is observed. The slightly higher modulus of the CDB can offer higher mechanical stability than that of the collagen type 1 hydrogel (figure 2(d)).

The vitreous body has a considerably aqueous environment, with approximately 98%–99% water [31]. As water compatibility is an essential property of biomaterials [32], we determined the swelling ratio of the CDB to the collagen type 1 hydrogel (figure 2(e)). The results showed that the CDB demonstrated higher water compatibility, indicating its suitability for cell activity and greater similarity to the vitreous body.

Replicating a microenvironment akin to *in vivo* conditions is essential when culturing tissue cells, including macrophages. To accomplish this, a range of hydrogels such as alginate, collagen, and hyaluronic acid are commonly employed [33]. To assess whether our CDB is more advantageous than these hydrogels for the growth and functional expression of macrophages, a comparative analysis involving alginate, CDB, and collagen was conducted (figures 2(f), (g) and S2).

We measured the biocompatibility between the bioink and macrophages, which are responsible for ocular immunity, among the few cells in the vitreous body (figure 2(f)). A live/dead assay was performed using macrophages on alginate, CDB, and collagen type 1 hydrogel. Encapsulated macrophages exhibited high viability over a 7 d period, indicating good biocompatibility of alginate, CDB, and collagen type 1 hydrogel. Furthermore, we observed that CDB surpassed other hydrogels in providing optimal support for macrophage survival, with macrophages maintaining a survival rate of over 98% even after 7 d (figure 2(g)). Additionally, to assess whether CDB offers enhanced support for macrophage function compared to other hydrogels, we conducted immunofluorescence staining and qRT-PCR analyses using samples collected at 7 d (figure S2). Since macrophages play crucial roles in phagocytosis, ocular immune privilege, cell migration and chemotaxis, and the production of vitreous-specific ECM [32, 34], experiments were conducted using the phagocytosis marker CD74, the ocular immune privilege marker TGF-β2, and the secreted vitreous ECM-specific marker SPP1. Immunofluorescence staining revealed significantly increased expression of all markers in CDB compared to alginate and collagen (figure S2(a)). These findings were further corroborated by qRT-PCR analysis (figure S2(b)). Thus, based on these results, we conclude that CDB is conducive to expressing the main functions of macrophages.

The light that passes through the cornea is transmitted through the vitreous body to the retina. Therefore, the vitreous body maintains a high transparency to reduce the loss of light transmitted to the retina [31]. Hence, ensuring material transparency is essential to create a vitreous-mimetic structure for studying light-induced pathological cell behavior and floater formation. Therefore, we measured the transparency of the CDB, collagen type 1, and alginate hydrogels, as well as that of the pure cdECM bioink. We did not encounter any difficulty while reading the printed letters through the evaluated bioinks (figure 2(h)). The measured transmittance results indicated that CDB exhibits over 60% transmittance across more than half of the visible spectrum (from 400 to 800 nm. However, while no significant variation was observed among all bioink, differences in transmittance were noted between each bioink and the natural vitreous body (figure 2(i)).

These results confirm that the developed CDB is appropriate for macrophage survival and functional expression, while exhibiting physical properties akin to those of other existing organ-derived dECM bioinks suitable for creating 3D structures, thereby maintaining adequate physical properties to uphold the 3D structure [34–36]. This also confirms the high transparency of CDB. Thus, CDB is a suitable biomaterial for fabricating vitreous-mimetic structures via 3D bioprinting.

3.2. Volumetric vitreous body printing

The vitreous body is the largest volumetric structure in the eye [1]. To recapitulate the volumetric structure of the vitreous body, we used the supporting bath–based extrusion printing method as it is suitable for layer-by-layer printing of a dECM bioink with weak mechanical properties for fabricating a high-aspect-ratio structure without a hard frame. In addition, as ensuring the transparency of the material in the vitreous structure is crucial, we conducted a transparency test for each CDB thickness to confirm the appropriate CDB-printed line thickness (figure 3(a)). As the CDB thickness decreased, the transmittance increased. CDB thicknesses exceeding 1000 μm resulted in a transmittance of less than 50%, rendering it impractical as a vitreous substitute (figure 3(b)). No significant differences in transmittance values were observed when the CDB thickness ranged from 400 to 700 μm, ensuring an adequate level of transparency as a vitreous substitute (figure 3(b)). However, an excessively thin CDB line may hinder maintaining the structural integrity, which is crucial for sustaining a stable 3D environment during culture to support appropriate cell function and withstand prolonged compression and fatigue loads that could contribute to floater formation. Hence, we proposed that a CDB line with a thickness of approximately 700 μm would offer a balance between transparency and strength.

Next, we analyzed the lines obtained from the best set of parameters for supporting bath–based print tuning (figure 3(c)). The optimized printing parameters included a pressure of 20 kPa and speed of 300 mm min^{-1}. The lines were well defined and stable, with an average thickness of 0.78 mm (figure 3(c)).

To fabricate a volumetric structure, material porosity should be considered to effectively diffuse oxygen and the components of the culture medium [37]. Thus, we designed a porous dome structure (Thin/Dome) with a diameter of 10 mm, height of 5 mm, layer thickness of 0.75 mm, and grid-like

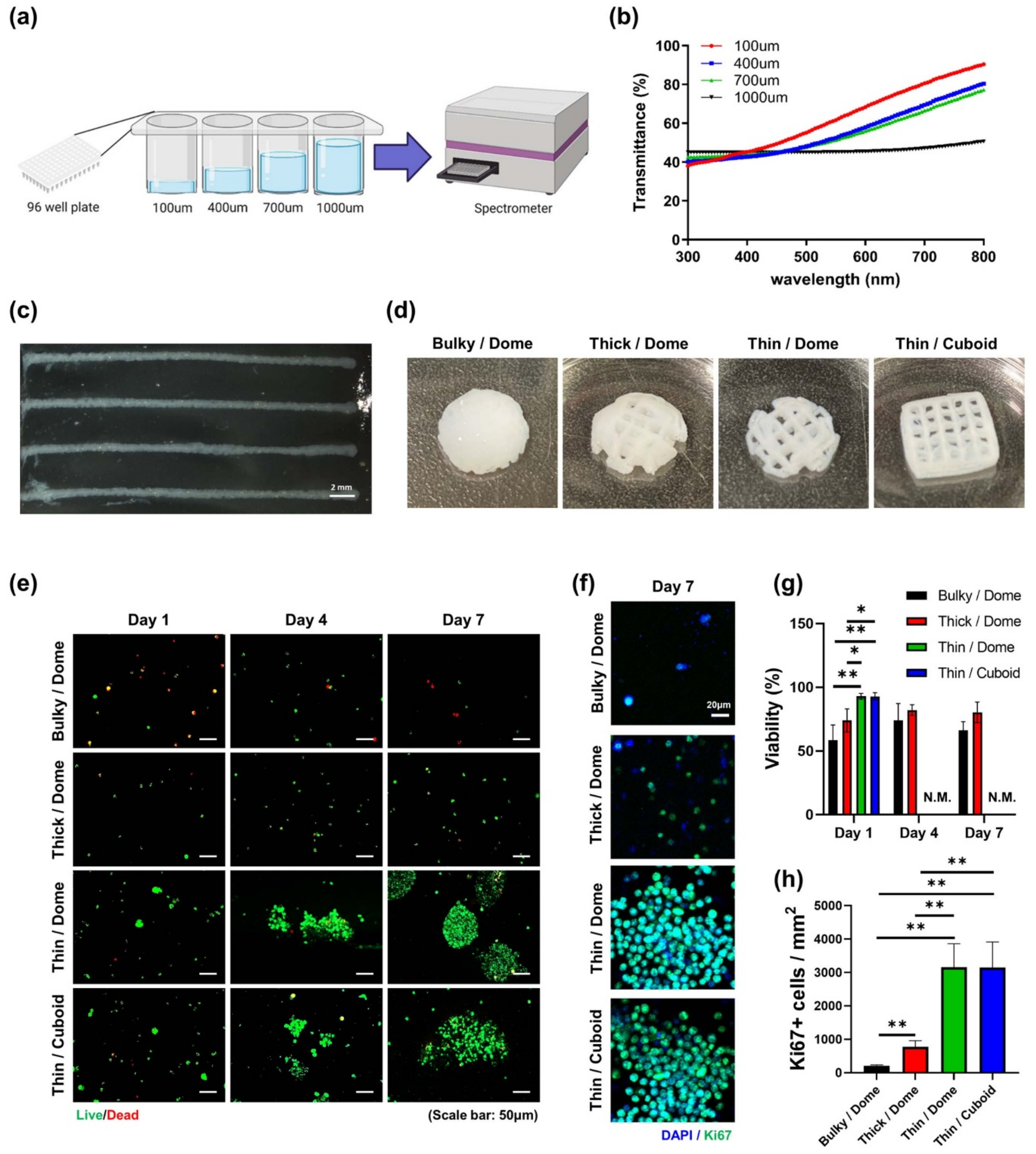

Figure 3. Fabrication and assessment of the porous dome for volumetric vitreous body simulation. (a) Schematic of the transparency measurement by CDB thickness. (b) Quantitative analysis of transmittance by CDB thickness. (c) Best-parameter -tuning test line for the CDB. (d) Printed structures, including the bulky/DOME, thick/dome, thin/dome, and thin/cuboid. (e) Live/dead assay images showcasing macrophages in the bulky/dome, thick/dome, thin/dome, and thin/cuboid structures on days 1, 4, and 7. (f) Immunostained images depicting Ki67 expression in the bulky/dome, thick/dome, thin/dome, and thin/cuboid structures on day 7. (g) Cell viability of macrophages based on the live/dead assay results for the bulky/dome, thick/dome, thin/dome, and thin/cuboid structures on days 1, 4, and 7 (N.M.: not measurable due to cells being too confluent). (h) Ki67-labled cell counting based on the immunostained images. The data are compared using student's t-test; the significant differences are indicated as follows: $^{*}p < 0.05$, $^{**}p < 0.01$, $^{***}p < 0.001$, and $\#p < 0.0001$ ($n = 3$). DAPI, $4'$,6-diamidino-2-phenylindole.

printing path (figure 3(d)). The distance between the lines was set to 2 mm. Reducing the line width to less than 0.78 mm easily destroyed the printed porous dome structure. Therefore, in this study, we set the line width to 0.78 mm at a feed rate of 300 mm min^{-1}, even though a thinner line may have increased the transparency.

To demonstrate the effectiveness of the porous dome structure (Thin/Dome) in volumetric vitreous body production, we compared the viability of macrophages inside the structures, including the bulky dome (Bulky/Dome), the porous dome with thick fiber (Thick/Dome), the porous dome with thin fiber (Thin/Dome), and the porous cuboid with thin fiber (Thin/Cuboid) (figure 3(d)). The Thick/Dome was 3D printed at a feed rate of 150 mm min^{-1}. In the compression test, the Bulky/Dome exhibited the highest mechanical strength, whereas the Thick/Dome displayed slightly higher mechanical strength than the Thin/Dome and Thin/Cuboid, which had similar mechanical properties (Fig. S3(a)). Live/dead assays conducted on days 1, 4, and 7 indicated significantly higher cell viability in the porous structures with thin fibers (Thin/Dome and Thin/Cuboid) than in the Bulky/Dome and Thick/Dome groups (figures 3(e) and (g)). A CCK assay was also performed to quantitatively assess cell viability, obtaining results consistent with those of the Live/Dead assay (figure S3(b)). Moreover, active proliferation and cluster formation of macrophages were observed in the Thin/Dome and Thin/Cuboid structures, whereas these phenomena were absent in the Bulky/Dome and Thick/Dome structures (figure 3(e)). Furthermore, the cell proliferation marker Ki67, which expresses the number of cells per mm^2, was notably higher in the Thin/Dome and Thin/Cuboid groups than in the Bulky/Dome and Thick/Dome groups (figures 3(f) and (h)). qRT-PCR analysis was performed on samples collected on day 7 to verify whether the Thin/Dome and Thin/Cuboid structures support cell functions more effectively than their Bulky/Dome and Thick/Dome counterparts (figure S3(c)). The analysis focused on markers such as the phagocytosis marker CD74, the cell migration and chemotaxis marker CXCL8, and the ocular immune privilege marker TGF-β2. Compared with the Bulky/Dome and Thick/Dome groups, the expression of all markers significantly increased in the Thin/Dome and Thin/Cuboid groups (figure S3(c)). These results suggest that the Thin/Dome and Thin/Cuboid structures may enhance the expression of key macrophage functions.

We additionally investigated the refractive index of the CDB 3D dome structure to evaluate its suitability as a vitreous body model. The refractive index of the native porcine vitreous body, CDB 3D dome structure without macrophages, and CDB 3D dome structure with macrophages were measured using a refractive index measurement machine. We found no significant difference in refractive index values between the native porcine vitreous body (1.3417 ± 0.0015), CDB 3D dome without macrophages (1.3397 ± 0.0061), and CDB 3D dome with macrophages (1.3447 ± 0.0098; figures S4(a) and (b)), indicating that the CDB 3D dome fabricated in this study is suitable as a vitreous body model in terms of the refractive index.

These observations indicate that the proposed porous design and 3D bioprinting strategy for fabricating a volumetric vitreous body enable stable cell culture conditions and advanced compatibility with optical devices for potential use in disease development and image analysis.

3.3. Feasibility of the fabricated volumetric vitreous body for eye model application

The transcriptional profile of hyalocytes differs from that of other myeloid cells such as macrophages, microglia, and monocytes. In contrast to other myeloid cells, hyalocytes exhibit unique characteristics in the vitreous body [38, 39]. Hyalocytes contribute to vitreous ECM protein synthesis, vitreous metabolism, homeostasis, and suppressing intraocular inflammation to ensure vitreous transparency [38, 40]. Therefore, the phagocytosis marker CD74, secreted vitreous ECM–specific marker SPP1, cell migration and chemotaxis regulatory markers CXCL8 and CX3CR1, and ocular immune privilege marker TGF-β2 are more prominent in hyalocytes than in other myeloid cells [40, 41]. By contrast, the CD68, a macrophage-specific marker, is expressed less in hyalocytes than in macrophages [41].

Based on the abovementioned difference between macrophages and hyalocytes, we confirmed the extent to which the encapsulated macrophages were similar to hyalocytes in the fabricated vitreous-mimetic structure and verified whether the fabricated vitreous-mimetic structure functioned as a vitreous body.

First, we fabricated a 2D structure in which the macrophages were cultured by coating the CDB on a petri dish. In addition, we fabricated 3D CDB bulky and porous dome structures containing macrophages via 3D bioprinting (figure 4(a)). Each construct was cultured for 7 d, and samples were obtained from each group (figure 4(b)).

We conducted qRT-PCR for each group using several markers, such as CD74, SPP1, CXCL8, CX3CR1, TGF-β2, and CD68 (figure 4(c)). We confirmed that all markers were expressed more in 3D structures than in 2D structures. In addition, cell mobility, ocular immune surveillance and privilege, and vitreous ECM synthesis were higher in the porous CDB dome than in the bulky CDB dome. By contrast, CD68 was found to be expressed less in the porous CDB dome than in the bulky CDB dome.

To confirm the qRT-PCR results, we performed immunofluorescence staining using CD74 and CD68 antibodies for each group (figure 4(d)). We confirmed that both CD74 and CD68 were expressed more in the 3D structures than in the 2D structures. However, the expression of CD74 and CD68 was higher and lower, respectively, in the porous CDB dome than in the bulky CDB dome. We also quantified the results of CD74 and CD68 fluorescence staining via fluorescence intensity analysis (figure 4(e)).

Additionally, to verify the ocular immune response of each structure, we treated each group with IFN-γ and LPS for 2 d to activate the macrophages (figure 4(b)). We collected the supernatant from each group 2 d after treatment and performed ELISA for TNF-α, IL-6, and CXCL8/IL-8 to confirm the amount of each cytokine released from each group (figure 4(f)). We confirmed that the released cytokine levels were higher in 3D structures than in 2D structures and in the CDB porous dome than in the CDB

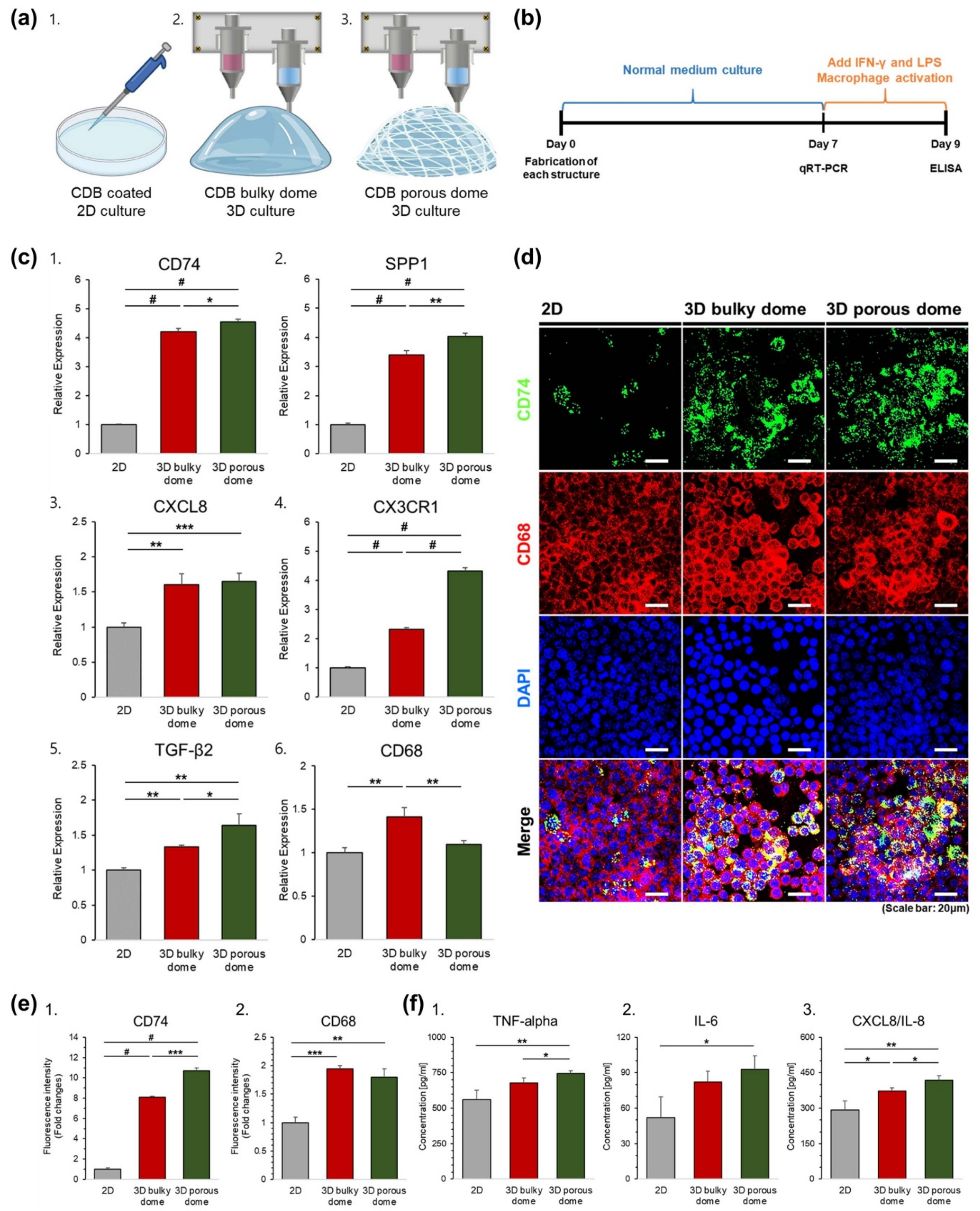

Figure 4. Biological quantitative evaluation of scaffolds appropriate for vitreous body mimicry. (a) Schematic of each structure according to the presence of pores and pore dimensions. (b) Schedule of the verification experiment for each fabricated structure. (c) *CD74, SPP1, CXCL8, CX3CR1, TGF-β2, and CD68* genes determined via qRT-PCR. (d) CD74 and CD68 immunofluorescence staining on day 7. (e) Fluorescence intensity analysis for CD74 and CD68. (f) Conformation of TNF-α, IL-6, and CXCL8/IL-8 released from each group using ELISA on day 7. The data are compared using student's t-test; the significant differences are indicated as follows: $^{*}p < 0.05$, $^{**}p < 0.01$, $^{***}p < 0.001$, and $\#p < 0.0001$ ($n = 3$). qRT-PCR, quantitative real-time polymerase chain reaction; ELISA, enzyme-linked immunosorbent assay; IL, interleukin; CXCL, C-X-C motif chemokine ligand 8; TNF-α, tumor necrosis factor-alpha; CX3CR, C-X3-C motif chemokine receptor 1 TGF-β, transforming growth factor-beta; 2D, two-dimensional; CDB, IFN-γ, interferon gamma; LPS, liposaccharide.

bulky dome. This indicated that the 3D CDB porous dome was the most suitable environment for maintaining vitreous immunity and vitreous-specific ECM production, similar to an actual vitreous body. We believe that the 3D CDB porous dome is highly effective for the following reasons: monocyte/macrophage lineage cells with high cell density in a limited space undergo apoptosis and various functional declines, including phagocytosis [32]. The 3D porous structure can secure the space for macrophage activity by aligning the cells with a high surface area. Moreover, the 3D porous structure increases the contact area between the cells and various chemicals included in the culture medium. Therefore, a 3D porous structure enhances cell–cell interactions and cell activity, resulting in improved phagocytic ability or cell migration of macrophages within the structure. In addition, the CDB in the 3D CDB porous dome constitutes a vitreous-specific microenvironment. Therefore, the 3D CDB porous dome can aid the macrophages in performing functions similar to those of hyalocytes.

Finally, we examined the suitability of the fabricated 3D CDB porous dome as both a disease model and a platform for drug testing by simulating vitritis. This condition, stemming from both infectious and non-infectious causes, significantly affects eye structures, such as the retina and cornea, requiring comprehensive inflammation therapy across the eye [42]. Corticosteroid treatment, which suppresses systemic inflammation, is often prioritized [43]. Thus, according to our planned protocol, we fabricated the 3D CDB porous dome and induced an acute immune environment by exposing it to a high dose of TNF-alpha to mimic vitritis. Subsequently, to assess the drug response of the disease model, we treated it with dexamethasone, a commonly used corticosteroid (figure S5(a)).

Exposure to TNF-alpha for two days led to the establishment of an acute inflammatory environment in the 3D CDB porous dome. Consequently, macrophages within the structure became highly activated, resulting in the overexpression of all macrophage-specific markers analyzed through immunofluorescence staining and qRT-PCR compared to their levels in the normal state (figures S5(b) and (c); Vitritis). The observations within the model mirror typical characteristics of vitritis, indicating the successful establishment of a vitreous disease model.

Following treatment of this vitritis model with dexamethasone for five days, an anti-inflammatory response was observed. The previously highly activated macrophages were subdued, leading to a significant decrease in the expression of all macrophage-specific markers, which reached levels similar to those observed in the normal state (refer to figures S5(b) and (c); Vitritis + Dexa). This response was confirmed through immunofluorescence staining and qRT-PCR. The observed reduction in expression levels suggests the effective therapeutic effect of the medication in the established vitritis model, as well as the potential application of the developed 3D CDB porous dome as a disease model and drug testing platform.

4. Discussion

In this study, we demonstrated that cdECM can be used for 3D vitreous body model printing and investigated supporting bath–based volumetric vitreous body printing technology to enhance transparency, cell viability, and hyalocyte-specific function of macrophages. The proposed porous dome structure, comprising fibers less than 1 mm thick, allowed light to reach the cells within the hydrogel while promoting suitable cell activity. This preliminary study on CDB and 3D porous design provided satisfactory results for eye model applications. In the future, we believe that the fabricated 3D porous structure may be used for vitreous disease research or for manufacturing more precise vitreous-like structures using hyalocytes.

Vitreous humor is a gel-like substance that occupies a major portion of the eye, dampens external forces, and plays a significant role in eye physiology. However, it undergoes natural aging in the form of liquefaction, resulting in the appearance of floaters, PVD, RD, and MHs, which can affect quality of life. Hyalocytes are macrophage-lineage cells residing in the vitreous body that play a role in the liquefaction of the vitreous body because of their role in the synthesis of collagen and hyaluronic acid. However, to study this disease, no 3D volumetric vitreous body or eye model replicating the aspects of synthesis and degradation of vitreous ECM has been developed. Furthermore, the 3D *in vitro* model has the advantages of recapitulating the 3D tension, 3D cell–matrix interaction, diffusion-based molecular transport, and 3D cell–cell interaction, causing discrepancies in how cells respond [44]. A 3D eye model incorporating a volumetric vitreous body can also facilitate testing cell response induced by 3D mechanical load transmission and light exposure.

3D bioprinting has become increasingly prevalent for producing 3D *in vitro* models. However, the progress in developing 3D volumetric vitreous body models has been limited owing to insufficient research on the appropriate bioink for the 3D cultivation of hyalocytes and ensuring printability within a vitreous body–specific microenvironment. When selecting a bioink, considering its composition is important as bioactive cues present in bioinks, such as binding sites and embedded soluble factors, can directly stimulate the cells, resulting in tissue morphogenesis [22]. Thus, in recent years, dECM has been widely used as a bioink, because it possesses several ECM proteins that work together synergistically to support tissue-specific cell function [45]. In this regard, vitreous body dECM bioink may provide an ideal environment to hyalocytes. However, the amount of dECM that can be extracted from the eye is too small to fabricate the bioink. Consequently, we found that a cartilage tissue is the most similar to the vitreous body among the materials reported in the literature [23]. For the first time, we demonstrated the cytocompatibility of cartilage dECM with macrophage-lineage cells.

Based on existing literature, we confirmed that cdECM and native cartilage have similar protein compositions, including enzymes [46, 47]. This similarity suggests that using CDB enables the creation of a microenvironment closely resembling that of a native vitreous body. By leveraging the advantageous characteristics of dECM bioink, we effectively applied CDB in the development of the vitreous body model. Additionally, previous studies have demonstrated the application of dECM from one tissue type to regenerate another. For instance, tendon dECM, placental tissue, and decellularized adipose tissue have been used, respectively, for nerve [48], skin [49, 50], and bone [51] regeneration. However, the total amount of each enzyme may differ between the native vitreous body and cdECM. Specifically, failing to carefully control the balance of complement enzymes can result in serious issues, such as ECM degradation or cell death, during the fabrication of vitreous substitutes. Therefore, to produce a precise vitreous substitute, the protein composition and total amount of the CDB must be controlled to a level similar to that of the native organ. Additionally, novel manufacturing methods and decellularization processes are necessary to match the physical properties and composition of the actual vitreous body. We plan to focus our research and attention on this topic in the future.

Supporting bath–based 3D bioprinting technology enables the 3D printing of hydrogels without a rigid frame [52–54]. However, the fabrication of a volumetric structure with a cell-encapsulating hydrogel and an interconnected porous structure is challenging in terms of maintaining the cell functionality and 3D shape during the culture. The developed CDB, parametric optimization study of supporting bath–based 3D printing, and porous dome design in this study enable the fabrication of a self-sustainable biologically functional volumetric tissue. We expect that the proposed strategy may be applied to the fabrication of other volumetric tissues.

The developed approach differs from the existing vitreous *in vitro* model fabrication method in that the biochemical and biophysical factors are simultaneously considered by fabricating a porous dome-shaped 3D structure using the CDB.

In previous studies on vitreous body mimicry, it was difficult to implement a specific microenvironment for vitreous cells by culturing in a 2D environment and using a single-component hydrogel [15–17]. Furthermore, previous studies on vitreous substitutes were mostly focused on the vitreous tamponade, and these hydrogel systems are unreliable as 3D scaffolds for hyalocytes, which are important for maintaining the physiology of the vitreous body. In addition, these hydrogels generally lack the capability to support appropriate cell behavior, even though these hydrogels are not cytotoxic. Furthermore, culturing cells in these hydrogels of large volumes poses a considerable challenge. To overcome these limitations, in this study, a porous 3D structure that enables the functions of vitreous cells was fabricated via 3D bioprinting, and a CDB that could simulate the vitreous-specific ECM environment was used. We evaluated the expression of various genes of vitreous cells, such as the phagocytosis, vitreous ECM-specific, and ocular immune privilege markers, and confirmed that the macrophages grown in the fabricated structure had functions similar to those of hyalocytes. The functions include vitreous ECM synthesis and the promotion of cell migration and proliferation. This signifies that the developed construct aids in expressing the function of vitreous cells by solving the problems of hypoxia and apoptosis and providing a microenvironment similar to that of the real vitreous body. In addition, in studies confirming the difference in functions of the existing monocyte/macrophage lineage cells, a large difference between the functions of the cells of a 2D culture and those obtained from actual humans [55, 56] was confirmed. Therefore, using the proposed 3D porous structure, which can provide a real vitreous environment and space, we expect to resolve the difference considerably.

Owing to the characteristics of the native vitreous body that allow light to pass through and reach the retina, constant refractive index and transparency are essential conditions for maintaining a vitreous body [28]. Therefore, for the developed CDB 3D dome to be suitable as a vitreous body model, it must have a refractive index and transmittance similar to that of a native human vitreous body. The actual refractive index of the human vitreous body is 1.341 [57]. The refractive index of the porcine vitreous body was similar to this value, and the measured values were consistent. This suggests that the CDB 3D dome fabricated in this study simulates the environment of an actual vitreous body well and is suitable as a vitreous body model.

The transmittance of the human vitreous body is below 60% for light wavelengths under 320 nm but exceeds 70% for light wavelengths over 320 nm [58]. We confirmed that the transmittance of the 3D CDB porcine structure for light with a wavelength of more than 500 nm was more than 80%. However, compared to the natural vitreous body, a disparity in transmittance remains, highlighting the need for future endeavors to slightly enhance transmittance. To achieve this, we will aim at manufacturing the vitreous substitute as thinly as possible while considering the refractive index. Furthermore, to fabricate an advanced eye model, further optimizations, such as increased transparency and improved biocompatibility with hyalocytes, will be the subject of future studies on floater formation and vitreous liquefaction. Moreover, the addition of retinal cells and retinal pigment epithelial cells in the vitreous body model will enable the study of the development of PVD, RD, and MH. In addition, as we used macrophages derived from monocyte cell lines, cells in the printed structure maintained their proliferation capacity during the culture. Thus, the developed model had higher cell counts than the native vitreous body, which may have harmful effects, such as inflammation and proliferative vitreoretinopathy, on the physiology of vitreous mimetics. Thus, to fabricate a more physiologically relevant model with low cell density, the adoption of primary macrophages or hyalocytes could be considered.

We successfully developed a model resembling vitritis, a vitreous disease, by subjecting the initially normal model to inflammatory substances. Moreover, we validated the efficacy of commercially available medication in this disease model. Consequently, the proposed disease model holds promise for investigating the mechanisms underlying hyalocyte-related inflammatory diseases, for exploring the development of novel treatments in the future and for supporting the creation of more diverse vitreous disease models. The function of the disease model can be verified by analyzing the gene expression pattern of hyalocytes obtained from this disease model, secretion pattern of inflammatory cytokines, and confirmation of the change patterns of hyalocyte activity [38, 40, 41]. Representative vitreous diseases are caused by viral invasion or autoimmune diseases, including vitritis [59]. Furthermore, most vitreous disorders, such as vitreoretinopathy and diabetic retinopathy, often involve other parts of the eye, such as the retina [60]. The main characteristics of these diseases are the formation of new blood vessels, disruption of the vascular endothelial barrier, and accumulation of macrophages in the blood vessels [34, 60]. Therefore, incorporating vascular mimetics into the developed disease model is essential to accurately simulate disease in the future.

Collagen type 1 promotes the EMT of epithelial cells when exposed to excessive immune or disease states, causing fibrosis or cancer [61]. However, under normal circumstances, collagen type 1 increases the function of normal epithelial cells; based on these characteristics, type 1 collagen is known to be frequently used as a coating material when growing HRPEs and HLEpiCs *in vitro* [62]. Therefore, to create a more precise model by adding a retina or lens to the developed eye model, it was necessary to confirm whether the CDB, which is rich in collagen type 1, does not cause the EMT of HRPEs and HLEpiCs. Through various experiments, we confirmed that collagen type 1 lowered the possibility of causing EMT in the cells and improved the cell function. Therefore, we verified that there were no problems in adding the retinal and lens components to the developed eye model using the CDB.

In conclusion, by adding the retinal and lens components as well as a vascular structure to the developed 3D structure, we expect to create more diverse *in vitro* ocular models and disease models, which may ultimately aid in the development of new treatments and research on ocular diseases for which the treatment is ambiguous.

5. Conclusion

In the present study, the CDB was investigated as a possible vitreous substitute in an eye model to study the formation of floaters and the development of vitreous liquefaction. We aimed to obtain a printable hydrogel bioink with adequate mechanical and biological properties and develop a 3D bioprinting process for volumetric vitreous body fabrication. The rheological analysis demonstrated the shear thinning behavior and thermal crosslinking, which are important for extrusion-based printing; furthermore, the swelling test showed high water compatibility of the developed structure. The CDB was found to be biocompatible, securing the viability of macrophages. Based on the correlation between transparency and gel thickness, the printing parameters were tuned to obtain a well-defined balance between transparency and mechanical stability. The chosen parameter set enabled the fabrication of a self-sustainable volumetric 3D porous structure without a rigid framework, and the porous design enabled the higher viability of macrophages and a greater transparency than that of the bulky gel. Finally, the printed volumetric vitreous body demonstrated the feasibility of eye model applications. By demonstrating that the macrophages in the 3D structure functioned similarly to hyalocytes, we confirmed that the 3D porous volumetric structures could act similarly as natural vitreous bodies. Finally, by inducing an acute inflammatory environment within a 3D porous volumetric structure, we created a disease model and validated its accurate response to commercial drugs. These findings suggest that the model is suitable to serve as a drug testing platform and to support personalized therapy research in the future.

Data availability statement

The data cannot be made publicly available upon publication because they are owned by a third party and the terms of use prevent public distribution. The data that support the findings of this study are available upon reasonable request from the authors.

Acknowledgments

The authors acknowledge the technical support of Dr Elena Mazzoldi from the Nocivelli Institute of the Spedali Civili of Brescia and the Department of Molecular and Translational Medicine of the University of Brescia. We thank BioRender (https://biorender.com/), an imaging platform that helped us create the schematic illustrations. We would like to thank Editage (www.editage.co.kr) for English language editing.

This study was supported by the National Research Foundation (NRF) of Korea grant funded by the Korea government (MSIP) (NRF-2022R1A2C3004300); Alchemist Project (20012378, Development of Meta Soft Organ Module Manufacturing Technology without Immunity Rejection and Module Assembly Robot System) funded By the Ministry of Trade, Industry & Energy (MOTIE, Korea).

Conflict of interest

The authors declare that they have no competing financial interests or personal relationships that may have influenced the work reported in this study.

Authors' contributions

J S K developed the concept. J S K, J J K and L R designed the experiments, and analyzed and interpreted the experimental data. J S K, J J K, and L R conducted the experiments. J S K, J J K and L R wrote the manuscript. P S L and D W C reviewed and edited the manuscript. P S L and D W C supervised the overall project. All authors have read and approved the final manuscript.

Funding

This study was supported by the National Research Foundation (NRF) of Korea grant funded by the Korea government (MSIP) (NRF-2022R1A2C3004300); Alchemist Project (20012378, Development of Meta Soft Organ Module Manufacturing Technology without Immunity Rejection and Module Assembly Robot System) funded By the Ministry of Trade, Industry & Energy (MOTIE, Korea).

ORCID iD

Dong-Woo Cho https://orcid.org/0000-0001-5869-4330

References

[1] Kokavec J, Min S H, Tan M H, Gilhotra J S, Newland H S, Durkin S R, Grigg J and Casson R J 2016 Biochemical analysis of the living human vitreous *Clin. Exp. Ophthalmol.* **44** 597–609

[2] Tram N K and Swindle-Reilly K E 2018 Rheological properties and age-related changes of the human vitreous humor *Front. Bioeng. Biotechnol.* **6** 199

[3] Angi M, Kalirai H, Coupland S E, Damato B E, Semeraro F and Romano M R 2012 Proteomic analyses of the vitreous humour *Mediators Inflamm.* **2012** 1–7

[4] Osmancevic A 2019 *Treating Vitreous Floaters with Nd:YAG Laser Vitreolysis* (University of Split School of Medicine. Ophthalmology)

[5] Donati S, Caprani S M, Airaghi G, Vinciguerra R, Bartalena L, Testa F, Mariotti C, Porta G, Simonelli F and Azzolini C 2014 Vitreous substitutes: the present and the future *Biomed. Res. Int.* **2014** 1–12

[6] Sebag J 2020 Vitreous and vision degrading myodesopsia *Prog. Retin. Eye Res.* **79** 100847

[7] Lin Q, Lim J Y, Xue K, Su X and Loh X J 2021 Polymeric hydrogels as a vitreous replacement strategy in the eye *Biomaterials* **268** 120547

[8] Levin M and Cohen N 2021 The effects of aging on the mechanical properties of the vitreous *J. Biomech.* **119** 110310

[9] Kalavar M, Hubschman S, Hudson J, Kuriyan A E and Sridhar J 2021 *Evaluation of Available Online Information regarding Treatment for Vitreous Floaters, Seminars in Ophthalmology* (Taylor & Francis) pp 58–63

[10] Broadhead G K, Hong T and Chang A A 2020 To treat or not to treat: management options for symptomatic vitreous floaters *Asia-Pacific J. Ophthalmol.* **9** 96–103

[11] Sakamoto T and Ishibashi T 2011 Hyalocytes: essential cells of the vitreous cavity in vitreoretinal pathophysiology? *Retina* **31** 222–8

[12] van Overdam K A, Busch E M, Verdijk R M and Pennekamp C W 2021 The role of vitreous cortex remnants in proliferative vitreoretinopathy formation demonstrated by histopathology: a case report *Am. J. Ophthalmol. Case Rep.* **24** 101219

[13] Halfter W, Sebag J and Cunningham E T 2014 II. E. Vitreoretinal interface and inner limiting membrane *Vitreous: In Health and Disease* (Springer) pp 165–91

[14] Sebag J 2009 Vitreous: the resplendent enigma *Br. J. Ophthalmol.* **93** 989–91

[15] Nuzzi R, Bergandi L, Zabetta L C, D'Errico L, Riscaldino F, Menegon S and Silvagno F 2020 In vitro generation of primary cultures of human hyalocytes *Mol. Vis.* **26** 818

[16] Matteucci A, Formisano G, Paradisi S, Carnovale-Scalzo G, Caiazza S, Hoerauf H and Malchiodi-Albedi F 2007 Biocompatibility assessment of liquid artificial vitreous replacements: relevance of *in vitro* studies *Surv. Ophthalmol.* **52** 289–99

[17] Tojo N, Kashiwagi Y, Nishitsuka K, Yamamoto S, Asao H, Sugawara N, Yamashita T, Yamamoto T and Yamashita H 2010 Interactions between vitreous-derived cells and vascular endothelial cells in vitreoretinal diseases *Acta Ophthalmol.* **88** 564–70

[18] Riva L, Mazzoldi E L, Ginestra P S, Ceretti E and Giliani S C 2022 Eye model for floaters' studies: production of 3D printed scaffolds *Prog. Addit. Manuf.* **7** 1–14

[19] Kačarević Ž P, Rider P M, Alkildani S, Retnasingh S, Smeets R, Jung O, Ivanišević Z and Barbeck M 2018 An introduction to 3D bioprinting: possibilities, challenges and future aspects *Materials* **11** 2199

[20] Fenton O S, Paolini M, Andresen J L, Müller F J and Langer R 2020 Outlooks on three-dimensional printing for ocular biomaterials research *J. Ocul. Pharmacol. Ther.* **36** 7–17

[21] Schulz A, Januschowski K and Szurman P 2021 Novel vitreous substitutes: the next frontier in vitreoretinal surgery *Curr. Opin. Ophthalmol.* **32** 288–93

[22] Kim B S, Das S, Jang J and Cho D-W 2020 Decellularized extracellular matrix-based bioinks for engineering tissue-and organ-specific microenvironments *Chem. Rev.* **120** 10608–61

[23] Lindberg G, Longoni A, Lim K, Rosenberg A, Hooper G, Gawlitta D and Woodfield T 2019 Intact vitreous humor as a potential extracellular matrix hydrogel for cartilage tissue engineering applications *Acta Biomater.* **85** 117–30

[24] Pati F, Jang J, Ha D-H, Kim S W, Rhie J-W, Shim J-H, Kim D-H and Cho D-W 2014 Printing three-dimensional tissue analogues with decellularized extracellular matrix bioink *Nat. Commun.* **5** 1–11

[25] Min K, Kong J S, Kim J, Kim J, Gao G, Cho D-W and Han H H 2022 Three-dimensional microfilament printing of a decellularized extracellular matrix (DECM) bioink using a microgel printing bath for nerve graft fabrication and the effectiveness of decm graft combined with a polycaprolactone conduit *ACS Appl. Bio Mater.* **5** 1591–603

[26] Eyre D 1991 *The Collagens of Articular Cartilage, Seminars in Arthritis and Rheumatism* (Elsevier) pp 2–11

[27] Jin Y, Lee J S, Kim J, Min S, Wi S, Yu J H, Chang G-E, Cho A-N, Choi Y and Ahn D-H 2018 Three-dimensional brain-like microenvironments facilitate the direct reprogramming of fibroblasts into therapeutic neurons *Nat. Biomed. Eng.* **2** 522–39

[28] Seo Y, Jung Y and Kim S H 2018 Decellularized heart ECM hydrogel using supercritical carbon dioxide for improved angiogenesis *Acta Biomater.* **67** 270–81

[29] Seo Y, Jeong S, Chung J J, Kim S H, Choi N and Jung Y 2019 Development of an anisotropically organized brain dECM hydrogel-based 3D neuronal culture platform for recapitulating the brain microenvironment *in vivo ACS Biomater. Sci. Eng.* **6** 610–20

[30] Rhee S, Puetzer J L, Mason B N, Reinhart-King C A and Bonassar L J 2016 3D bioprinting of spatially heterogeneous collagen constructs for cartilage tissue engineering *ACS Biomater. Sci. Eng.* **2** 1800–5

[31] Swindle K E and Ravi N 2007 Recent advances in polymeric vitreous substitutes *Expert Rev. Ophthalmol.* **2** 255–65

[32] Jang J, Lee J, Seol Y-J, Jeong Y H and Cho D-W 2013 Improving mechanical properties of alginate hydrogel by reinforcement with ethanol treated polycaprolactone nanofibers *Composites* B **45** 1216–21

[33] Bae M, Kim J J, Kim J and Cho D-W 2024 Decellularized extracellular matrix for three-dimensional bioprinted *in vitro* disease modeling *Int. J. Bioprinting* **10** 1970

[34] Kim J J, Park J Y, Nguyen V V T, Bae M, Kim M, Jang J, Won J Y and Cho D W 2023 Pathophysiological reconstruction of a tissue-specific multiple-organ on-a-chip for Type 2 diabetes emulation using 3D cell printing *Adv. Funct. Mater.* **33** 2213649

[35] Bae M, Ko M K, Jin Y, Shin W J, Park W, Chae S, Lee H J, Jang J, Yi H-G and Lee D S 2021 Neural stem cell delivery using brain-derived tissue-specific bioink for recovering from traumatic brain injury *Biofabrication* **13** 044110

[36] Kim H, Park M-N, Kim J, Jang J, Kim H-K and Cho D-W 2019 Characterization of cornea-specific bioink: high transparency, improved *in vivo* safety *J. Tissue Eng.* **10** 2041731418823382

[37] Choi Y-J, Jun Y-J, Kim D Y, Yi H-G, Chae S-H, Kang J, Lee J, Gao G, Kong J-S and Jang J 2019 A 3D cell printed muscle construct with tissue-derived bioink for the treatment of volumetric muscle loss *Biomaterials* **206** 160–9

[38] Boneva S K, Wolf J, Wieghofer P, Sebag J and Lange C A 2022 Hyalocyte functions and immunology *Expert Rev. Ophthalmol.* **17** 249–62

[39] Lazarus H S and Hageman G S 1994 In situ characterization of the human hyalocyte *Arch. Ophthalmol.* **112** 1356–62

[40] Wolf J, Boneva S, Rosmus -D-D, Agostini H, Schlunck G, Wieghofer P, Schlecht A and Lange C 2022 Deciphering the molecular signature of human hyalocytes in relation to other innate immune cell populations *Invest Ophthalmol. Vis. Sci.* **63** 9

[41] Boneva S K, Wolf J, Rosmus -D-D, Schlecht A, Prinz G, Laich Y, Boeck M, Zhang P, Hilgendorf I and Stahl A 2020 Transcriptional profiling uncovers human hyalocytes as a unique innate immune cell population *Front. Immunol.* **11** 567274

[42] Jiang A, Wang J, Joshi M and Christoforidis J B 2013 Systemic treatments for noninfectious vitreous inflammation *Mediators Inflamm.* **2013** 1–11

[43] Sabrosa N A and Pavésio C 2000 Treatment strategies in patients with posterior uveitis *Int. Ophthalmol. Clin.* **40** 153–61

[44] Kong J S, Huang X, Choi Y J, Yi H G, Kang J, Kim S, Kim J, Lee H, Rim Y A and Ju J H 2021 Promoting long-term cultivation of motor neurons for 3D neuromuscular junction formation of 3D *in vitro* using central-nervous-tissue-derived bioink *Adv. Healthcare Mater.* **10** 2100581

[45] Kim J J, Bae M, Kim J and Cho D-W 2024 Application of biomaterial-based three-dimensional bioprinting for organ-on-a-chip fabrication *Int. J. Bioprinting* **10** 1972

[46] Visscher D O, Lee H, van Zuijlen P P, Helder M N, Atala A, Yoo J J and Lee S J 2021 A photo-crosslinkable cartilage-derived extracellular matrix bioink for auricular cartilage tissue engineering *Acta Biomater.* **121** 193–203

[47] Aretz S, Krohne T U, Kammerer K, Warnken U, Hotz-Wagenblatt A, Bergmann M, Stanzel B V, Kempf T, Holz F G and Schnölzer M 2013 In-depth mass spectrometric mapping of the human vitreous proteome *Proteome Sci.* **11** 1–10

[48] Yan L, Liu S, Wang J, Ding X, Zhao Y, Gao N, Xia Z, Li M, Wei Q and Okoro O V 2024 Constructing nerve guidance conduit using DECM-doped conductive hydrogel to promote peripheral nerve regeneration *Adv. Funct. Mater.* 2402698

[49] Bashiri Z, Fomeshi M R, Hamidabadi H G, Jafari D, Alizadeh S, Bojnordi M N, Orive G, Dolatshahi-Pirouz A, Zahiri M and Reis R L 2023 3D-printed placental-derived bioinks for skin tissue regeneration with improved angiogenesis and wound healing properties *Mater. Today Bio* **20** 100666

[50] Roy A, Mantay M, Brannan C and Griffiths S 2022 Placental tissues as biomaterials in regenerative medicine *Biomed Res. Int.* **2022** 6751456

[51] Ahn W B, Lee Y B, Ji Y-H, Moon K-S, Jang H-S and Kang S-W 2022 Decellularized human adipose tissue as an alternative graft material for bone regeneration *Tissue Eng. Regen. Med.* **19** 1089–98

[52] McCormack A, Highley C B, Leslie N R and Melchels F P 2020 3D printing in suspension baths: keeping the promises of bioprinting afloat *Trends Biotechnol.* **38** 584–93

[53] Noor N, Shapira A, Edri R, Gal I, Wertheim L and Dvir T 2019 3D printing of personalized thick and perfusable cardiac patches and hearts *Adv. Sci.* **6** 1900344

[54] Lee A, Hudson A, Shiwarski D, Tashman J, Hinton T, Yerneni S, Bliley J, Campbell P and Feinberg A 2019 3D bioprinting of collagen to rebuild components of the human heart *Science* **365** 482–7

[55] Januschowski K, Schnichels S, Hurst J, Hohenadl C, Reither C, Rickmann A, Pohl L, Bartz-Schmidt K-U and Spitzer M S 2019 Ex vivo biophysical characterization of a hydrogel-based artificial vitreous substitute *PLoS One* **14** e0209217

[56] Stein S, Bogdahn M, Rosenbaum C, Weitschies W and Seidlitz A 2017 Distribution of fluorescein sodium and triamcinolone acetonide in the simulated liquefied and vitrectomized vitreous model with simulated eye movements *Eur. J. Pharm. Sci.* **109** 233–43

[57] Ruggeri M, Uhlhorn S R, De Freitas C, Ho A, Manns F and Parel J-M 2012 Imaging and full-length biometry of the eye during accommodation using spectral domain OCT with an optical switch *Biomed. Opt. Express* **3** 1506–20

[58] Brockmann C, Schulz M and Laube T 2008 Transmittance characteristics of ultraviolet and blue-light-filtering intraocular lenses *J. Cataract Refract. Surg.* **34** 1161–6

[59] Selmi C 2014 Diagnosis and classification of autoimmune uveitis *Autoimmun. Rev.* **13** 591–4

[60] Kroll P, Büchele Rodrigues E and Hoerle S 2007 Pathogenesis and classification of proliferative diabetic vitreoretinopathy *Ophthalmologica* **221** 78–94

[61] Hay E D 1995 An overview of epithelio-mesenchymal transformation *Cells Tissues Organs* **154** 8–20

[62] Lu J T, Lee C J, Bent S F, Fishman H A and Sabelman E E 2007 Thin collagen film scaffolds for retinal epithelial cell culture *Biomaterials* **28** 1486–94